Experimental study of double cavity flow

F. Tuerke · L. R. Pastur · D. Sciamarella · F. Lusseyran · G. Artana

Abstract The flow through two facing, identical cavities (double cavity) is characterized experimentally, as the inflow velocity and the distance between the cavities is varied. Standard 2D2C particle image velocimetry measurements in the spanwise mid-plane provide information on the instantaneous and mean velocity flow fields. Laser Doppler velocimetry measurements at several points in the double cavity domain reveal the global character of the streamwise fluctuating velocity spectra. The flow is characterized based on times series, recorded in one of the cavity's shear layer, for a wide range of inflow velocities and intercavity distances. In a detailed spectral study we show, how the shear layer spectra get affected when the two cavities are brought closer together. Based on the the experimental data a temporal local linear stability analysis was carried out, which was able to explain why the frequency peaks for close intercavity distances broaden and move to higher Strouhal numbers.

F. Tuerke[1] · G. Artana
Departamento de Ingeniería Mecánica,
Universidad de Buenos Aires, CABA, Argentina
CONICET - Consejo Nacional de Investigaciones
Científicas y Técnicas, Argentina
[1] E-mail: ftuerke@fi.uba.ar

L. R. Pastur · D. Sciamarella · F. Lusseyran
LIMSI-CNRS, BP 133, F-91403 Orsay Cedex, France

F. Tuerke · L. R. Pastur · F. Lusseyran
Université Paris Sud XI (Paris-Saclay) Orsay Cedex, France

1 Introduction

Flows past cavities are known to generate self-sustained oscillations, which are of great practical, as well as academic interest, and have been studied extensively over the past decades experimentally [1–3], numerically [4, 5], as well as theoretically [6–9], ranging from subsonic to supersonic flow conditions. Fluid dynamic oscillations are attributed to instabilities arising from the cavity's shear layer and are enhanced through a feedback mechanism, which organizes the flow globally. In the literature, the feedback is described by a variety of different view-points, ranging from the flow acoustic feedback mechanism (commonly known as the *Rossiter* mechanism [10]) in compressible flows to hydrodynamic feedback [11,12] and reflected instability waves [9] in incompressible flows.

Double cavity flow arises when a fluid flows through two identical cavities which are facing each other in a symmetrical setup as in Ref. [13]. The geometry is found in nature as well as engineering applications and is therefore of interest to a large variety of fields: the sudden expansion and contraction in pipe flows, river flows, the flow through arteries with obstacles and the laryngeal ventricle or Morgagni's sinus in the human phonatory system [13] are some of numerous examples of double cavity flow.

Historically, the study of linear stability of the flow over single open cavities has been focused on the self-sustained oscillations of the predominantly two dimensional shear layer [14,15]. Only in recent years, computationally more expensive three dimensional linear stability analysis have become available [5,16,17], mostly focusing on the three dimensional structures (*e.g.* centrifugal instabilities) of the inner flow.
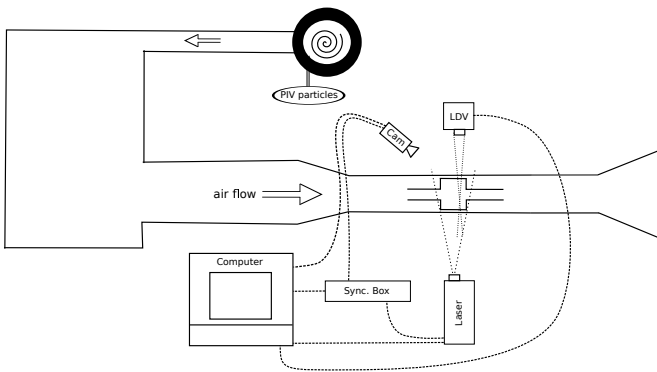
Fig. 1: The subsonic open wind tunnel setup at LIMSI-CNRS.

Fig. 2: Sketch of experimental setup: Three dimensional double cavity geometry of distance D, length L, depth H, spanwise extension S and inflow velocity U_∞ with horizontal laser sheet in the mid-plane ($y = 0$) and camera position.

In their landmark paper on open cavity flow, Rockwell and Naudascher [15] mention the double cavity ("axis-symmetrical internal cavity"), though little attention has been given so far to this geometry in the incompressible limit when intermediate to large intercavity distances are considered. Previous works on the double cavity geometry, found in the literature, such as *e.g.* Maurel et al. [18], focus on very close intercavity distances, low Reynolds numbers and on the effect of varying the cavity length, rather than the distance between the cavities. The result is an impinging jet of changing length and speed. Morel [19] studies an axis-symmetric double cavity but for high subsonic Mach numbers, applying the Rossiter mechanism.

In the present work, we address double cavity flow of varying intercavity distances and inflow velocity in the incompressible limit and focus on the coupling of the shear layers, that develop over both cavities. The double cavity is not axis symmetric, but symmetric with respect to the mid-plane. Hence, our study fills the missing gap between the studies by Ref. [18] (planar jet) and the other extreme, namely open cavity flow (as *e.g.* in Ref. [1]). We study the flow field using particle image velocimetry (PIV) and obtain detailed spectral information at discrete points in the flow field from laser Doppler velocimetry (LDV) measurements for a wide range of parameters. Based on the experimental data of the mean velocity fields, a local temporal linear stability analysis is performed, which seeks to study the dominant dynamics of the shear layer interactions. The results of the instability analysis are compared to the experimental spectra of the streamwise velocity fluctuations.
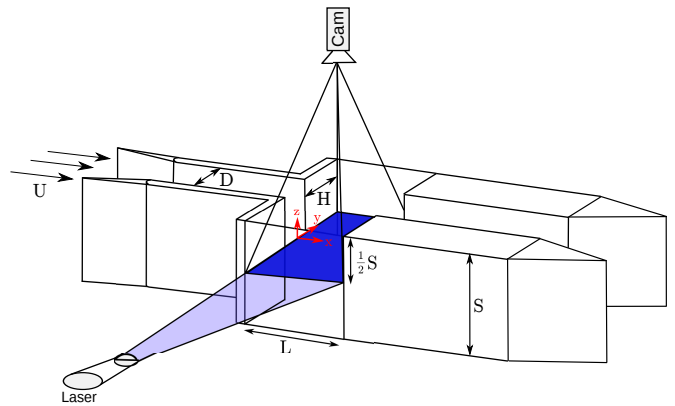
2 Experimental setup

2.1 Wind tunnel

The study was carried out in the open wind tunnel of LIMSI-CNRS, schematically depicted in figure 1. The wind tunnel facility is composed of a centrifugal fan, providing stationary volume flow, a settling chamber that contributes to equalize the flow and a honey-comb panel, placed at the inlet of the contraction, which contributes to laminarize the flow. The double cavity geometry is placed in the test section as schematically depicted in perspective view in figure 2, and in top view in figure 3. The profiled and by approximately 4 degrees inclined leading edges separate the flow into two bypass streams, one at either side of the geometry, and a center flow entering the inflow channel leading to the double cavity test section. Consequently, two, with respect to the double cavity center line symmetrical, laminar boundary layers are created, that develop in a 170 mm-long inflow channel, before entering the double cavity. The wind tunnel walls, as well as the double cavity side wall, are made of 2 mm-thick reflection-treated glass, allowing for complete optical access. The rest of the double cavity geometry is made of acrylic Plexiglas. Adaptable shields are mounted at the test section outlet, as well as at the wind tunnel outflow, in order to minimize perturbations of the inflow.

The cavity ratio $\Gamma = L/H = 2$ is kept constant throughout the entire study. The intercavity distance D is varied from $D/L = 0.1$ to $D/L = 1$. The cavity length $L = 50\,\mathrm{mm}$, as well as the inflow length and the outflow length, are kept constant at $L_1 = 3.4L$ and $L_2 = 2.6L$,
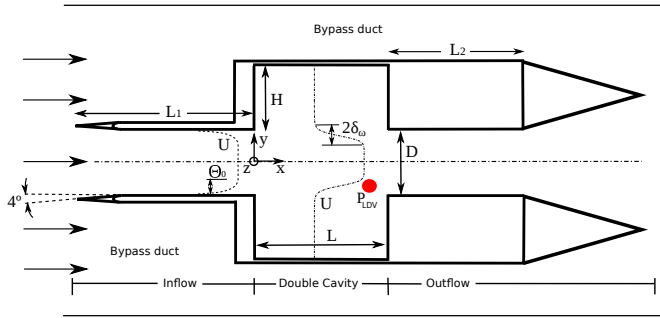
Fig. 3: Top view of figure 2. Double cavity geometry with variable distance $5 \leq D \leq 50\,\text{mm}$, constant length $L = 50\,\text{mm}$, constant depth $H = 25\,\text{mm}$, constant spanwise extension $S = 75\,\text{mm}$, constant inflow and outflow channel length $L_1 = 170\,\text{mm}$ and $L_2 = 130\,\text{mm}$, respectively, and variable inflow velocity U_∞. The red filled circle indicates the main LDV probe point at $P_{\text{LDV}} = [45\text{mm}, 5\text{mm}]$. The inflow velocity profile $(--)$ with the center velocity U_∞ and the momentum thickness Θ_0 and the double cavity profile $(-\cdot-)$ with the shear layer thickness δ_ω are depicted.

Table 1: Summary of cases

Cases	D [mm]	D/L [-]	Symbol
DC05	5	0.1	+
DC10	10	0.2	▼
DC15	15	0.3	○
DC20	20	0.4	△
DC25	25	0.5	×
DC30	30	0.6	◁
DC40	40	0.8	◇
DC50	50	1.0	►
SC50	50	1.0	□

respectively. The spanwise extension is kept constant at $S = 1.5L$, limited by the floor and the ceiling of the wind tunnel. As a reference, a single cavity case is added to the double cavity cases, by closing one of the two facing cavities at a distance of $D/L = 1$. A Cartesian coordinate system is $(\mathbf{e}_x, \mathbf{e}_y, \mathbf{e}_z)$ is set midspan at the cavity leading corner, as shown in figures 2 and 3. The study concerns Reynolds numbers between $Re_L \approx 3\,000$ and $Re_L \approx 14\,800$, where the Reynolds number, based on the cavity length and the maximum velocity in the inflow channel, is defined as

$$Re_L = \frac{U_\infty L}{\nu} \qquad (1)$$

with $\nu = 15 \cdot 10^{-6}\,m^2/s$ being the dynamic viscosity of air at room temperature (24 degrees Celsius). Due to a geometrically induced limited translucency at $-0.2 \lesssim x/L \lesssim 0$, the maximum inflow velocity profile U_∞ is taken slightly upstream of the entry to the double cavity at $x/L = -0.3$. The momentum thickness Θ_0 is obtained at the same x-position. The total turbulent intensity on the inflow channel center line was measured as to less than 1% in all cases.

2.2 PIV and LDV

Standard two component (2D2C) particle image velocimetry (PIV) and laser Doppler velocimetry (LDV) are carried out simultaneously. The PIV system consists of a CCD camera, a laser system, a synchronization box and a personal computer (PC), as shown in

figure 1. The DALSA Genie Camera is equipped with a FUJINON $1:1.8/50\,\text{mm}$ lens and records images with a resolution of 1368×1024 pixels, which are encoded in 8 bits, saved and post-processed on a PC. The light source, which is synchronized by a synchronization box with the camera, is a Quantel Laser from Big Sky Laser Tech., Inc. Model PIV190 PS2, that sends two laser pulses with a time difference of Δt. The wave length of the lasers is $\lambda = 532\,\text{nm}$, providing a maximum energy output of $2 \times 190\,\text{mJ}$ in the green part of the visible light spectrum. The lasers are set to pulsate at its maximum rate of 15 Hz, with each pulse lasting roughly $10\,\text{ns}$. The light pulses are projected into a horizontal plane by a concave lens, creating a laser sheet at $z/S = 0$ as shown in figure 2. In this plane the displacement vector $\mathbf{\Delta x} = [\Delta x, \Delta y]^\intercal$, together with the known time difference between the two laser pulses, Δt, yield the velocity vector $\mathbf{u} = \mathbf{\Delta x}/\Delta t = [u, v]^\intercal$. The time difference Δt varies between $275\,\mu\text{s}$ and $700\,\mu\text{s}$, depending on the inflow velocity. Seeding particles are liquid droplets of mineral oil DEHS – di(2-ethylhexyl)sebacate –, sprayed at the fan entrance. DEHS density is 0.9 and droplet diameter are of the order of $1\,\mu m$. Measurements start only after the seeding particle distribution is uniform inside the double cavity. The field of vision is adapted, such that for all intercavity distances the complete double cavity area is covered. The PIV measurement plane is kept constant in the symmetry plane at $z/S = 0$. After image pre-processing, including mean field subtraction as well as intensity corrections, displacement fields are computed using a FFT based cross-correlation algorithm of two corresponding interrogation windows, that are consecutively decreased from 64×64 pixels down to 8×8 pixels in size, using a 50% overlap. For each case 400 images, resulting in 200 instantaneous vector fields, are recorded. The mean was found to be well converged after around 120 fields.

LDV measurements, using a Dantec BSA-system, are performed simultaneously with the PIV measure-

ments. A continuous argon-ion laser (35 mW), with a wave length of 660 nm, is used. In the main probe point P_{LDV}, located 5 mm upstream and 5 mm above the trailing edge, as indicated in figure 3, the streamwise velocity component u is recorded. As also found by [1], in the vicinity of P_{LDV}, shear layer oscillations are of highest amplitude, while low frequency content of the recirculation region is still present, but not dominant. LDV series are recorded over 30 seconds for each case, at a LDV count rate of the order of 3 kHz. Time series are resampled at the mean particle sampling frequency by linear interpolation before performing Fourier analysis. The power spectral density (PSD) of a time series is obtained by the help of the Welch algorithm [20] using an overlapped segment averaging estimator with a Hamming window size equal to 5.2 seconds and a segment overlap of 98%. One LDV recording hence consists of roughly 260 windows for averaging. The resulting frequency resolution is $\Delta f = 0.18$ Hz. With these parameters the 95% confidence interval is found below [$\pm \simeq 1.30$dB]. Throughout this work the PSD is normalized according to $P = 2PSD\Delta f$ and is presented in Decibel units ($20\log_{10}(P)$ [dB]). The non-dimensional frequency (Strouhal number)

$$St_L = \frac{fL}{U_\infty} \tag{2}$$

is used to graphic the data.

3 Double cavity flow

3.1 Flow description

Table 1 summarizes the cases under study. Eight double cavity (DC) cases with different intercavity distances D are complemented by a single cavity case (SC) as a reference in the limit $D \to \infty$. The instantaneous flow fields (see videos provided in supplementary material) of cases with $7\,000 \lesssim Re_L \lesssim 8\,000$ show that for $D/L \geq 0.2$, the center flow separates the two cavities in such a way that no fluid is exchanged. At the smallest distance ($D/L = 0.1$), the center flow starts to oscillate and fluid is alternately spilled into the cavities. This flapping jet enforces the intracavity recirculation region, resulting in a destabilizing effect on the center flow. This type of flow is commonly refered to as *confined jet* flow in the literature [18].

The mean flow is shown in figure 4, for two intracavity distances, at approximately the same Reynolds number. In each cavity the recirculation region is structured into a main vortex, occupying most of the cavity, and a second smaller one, located further upstream.
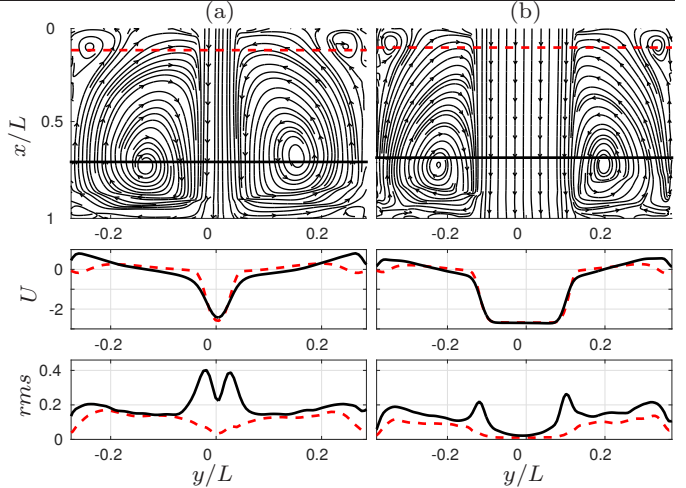

Fig. 4: Mean flow fields. Top row: Streamlines over the time averaged field for double cavity cases (a) $D/L = 0.1$ and (b) $D/L = 0.5$ both at $Re_L \approx 8\,700$. Flow from top to bottom. Middle row: Mean velocity profiles at $x/L = 0.1$ (red $--$) and at $x/L = 0.7$ (black —). Buttom row: rms profiles at $x/L = 0.1$ (red $--$) and at $x/L = 0.7$ (black —).
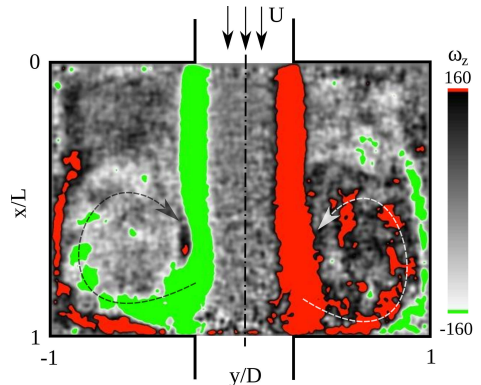

Fig. 5: Contour plot of spanwise instantaneous vorticity $\omega_z = \partial_x v - \partial_y u$, computed from the 30 most energetic POD modes of the velocity field. Double cavity configuration with $D/L = 0.4$ at $Re_L \approx 8900$. Flow from top to bottom.

Figure 4 also shows the streamwise mean velocity profiles and the root mean square (rms) profiles at the indicated streamwise positions. Comparing the inflow profiles (at $x/L \approx 0.1$) with the profiles in the rear cavity part (at $x/L \approx 0.7$), we note that the velocity profile in the channel center is independent of the streamwise position, whereas the intracavity flow is more pronounced at the location further downstream. The profiles of the rms show, that two shear layers are formed along the cavity. For small intercavity distances (figure 4(a)), the two shear layers join in the downstream part of the
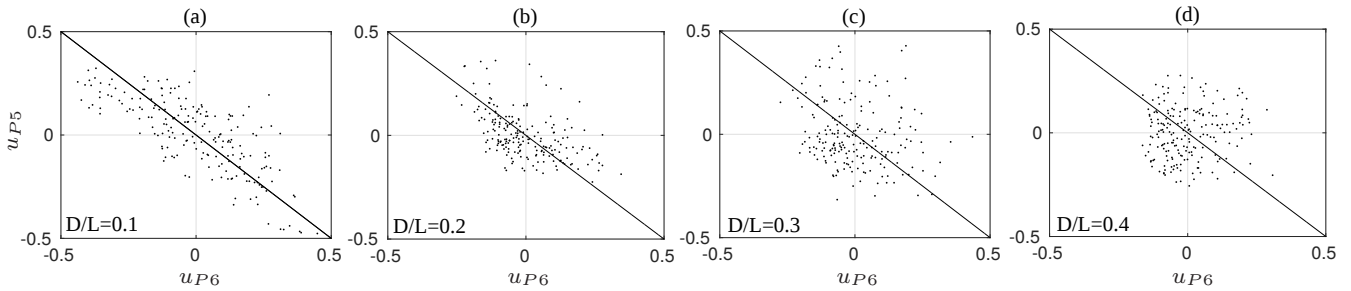
Fig. 6: Fluctuating streamwise velocity correlations of shear layer probe points (*cf.* figure 11) at a streamwise position $x_{P5} = x_{P6} = 0.6\,L$ and $y_{P5,P6} = \pm D/2$ for (a) $D/L = 0.1$, (b) $D/L = 0.2$, (c) $D/L = 0.3$ and (d) $D/L = 0.4$. The Reynolds number range is $5\,000 \lesssim Re_L \lesssim 6\,000$.

domain, forming a jet. For larger intercavity distances (figure 4(b)), the two shear layers stay separate all along the cavity length.

Figure 5 shows a typical instantaneous field of the spanwise vorticity component $\omega_z = \partial_x v - \partial_y u$ of a $D/L = 0.4$ case at $Re_L \approx 8\,900$. The vorticity field was computed from the 30 most energetic POD (proper orthogonal decomposition) modes of the velocity field. Both shear layers, originating from the boundary layers of the inflow channels, can clearly be distinguished. When the shear layers impinge on the cavity rear edge, vorticity is regularly injected into the respective cavities. The injected vorticity forms small vortices at the frequency of the shear-layer oscillations. These regularly spaced vortices, that circumvent along a dipolar vortex sheet inside each cavity, were also observed by Ref. [1] for the case of the single cavity. Recently, Ref. [12] showed by means of two dimensional numerical simulations of double cavity flow, that the small vortex structures create a hydrodynamic feedback mechanism which is responsible for the appearance of non-harmonic frequency peaks.

In order to elucidate the spatio-temporal symmetry characteristics of the facing cavities, figure 6 shows the spatial correlation graphs of the streamwise fluctuating velocity component $u = \mathbf{u}\mathbf{e}_x - \langle \mathbf{u}\mathbf{e}_x \rangle_t$ between two shear layer points $P_5 = [x_{P5}, y_{P5}]$ and $P_6 = [x_{P6}, y_{P6}]$ (see caption of figure 6 for details), for the four closest intercavity distances $0.1 \lesssim D \lesssim 0.4$. At $D/L = 0.1$ the flow is globally anti-symmetric from a spatio-temporal point of view, as can be seen from the elongated cloud of points, spread along the diagonal in figure 6(a). At $D/L = 0.2$ the flow is still mainly anti-symmetric, however, with increasing distance 6(c)-(d), the cloud of points transforms from the elongated form to a circular form. The distribution of the points becomes aleatory, indicating that the correlation and hence the symmetry is lost.
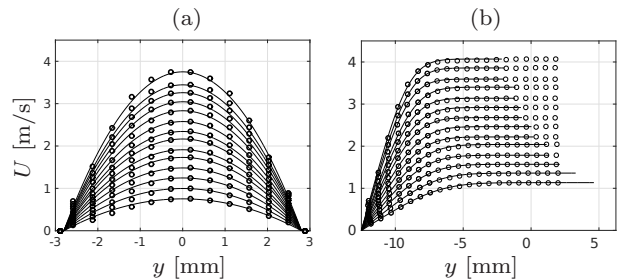

Fig. 7: Experimental and analytical velocity profiles at inflow position $x = -0.03$ for cases at (a) $D/L = 0.1$ (parabolic fit) and at (b) $D/L = 0.5$ (Blasius boundary layer fit).

3.2 Velocity profiles

The incoming boundary layer is obtained at position $x/L = -0.3$. Depending on the inflow velocity and the intercavity distance the streamwise inflow profile $U(y)$ either corresponds to a parabolic profile of the form

$$U_p(y) = U_\infty \left(1 - \frac{y^2}{D^2} \right) \qquad (3)$$

or to a symmetric (double) Blasius boundary layer profile. The parabolic profile is obtained when the two opposing boundary layers join in the channel center. This happens for all cases at the distance $D/L = 0.1$ and for the lower Reynolds number cases at the distance $D/L = 0.2$. The parabolic fit, together with experimentally measured profiles for all cases at $D/L = 0.1$, are shown in figure 7(a). A good agreement between the analytic profiles and the experimental profiles is observed. For all other distances, the Blasius boundary layer is fitted to the experimental data. The fits are performed by minimizing the $\mathcal{L}_2$-norm difference of experimental streamwise velocity profile and the analytical profile. The results for the distance $D/L = 0.5$ are exemplified in figure 7(b). A good agreement between experiments and analytical profile was found for
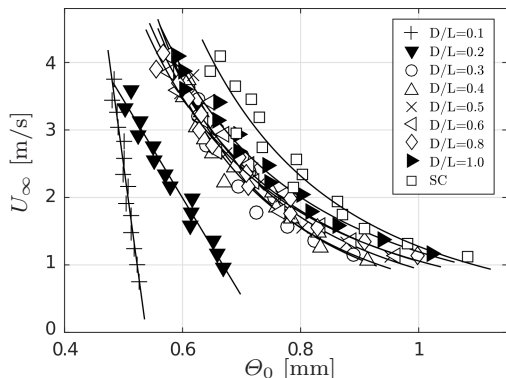
Fig. 8: Momentum thickness of incoming boundary layer Θ_0, measured at $x = 0.03\,\mathrm{m}$ for all cases in table 1. Symbols show experimental data and solid lines (——) indicate least square fits.

all inflow velocities. The shape factors of the profiles vary between 2.62 and 2.72, strongly suggesting a laminar inflow. The shear layers, that form upon separation at the double cavity's leading edge, depend on the momentum thickness Θ_0 of the incoming velocity profile. The momentum thickness is calculated according to

$$\Theta_0 = \int_0^\infty \frac{U(y)}{U_\infty}\left(1 - \frac{U(y)}{U_\infty}\right) dy \qquad (4)$$

Figure 8 shows the momentum thickness Θ_0, calculated from experimental data, for all cases in table 1, as a function of the center line inflow velocity U_∞. For the parabolic profiles the momentum thickness is in theory independent of the center line velocity U_∞ and depends only on the intercavity distance. At $D/L = 0.1$ an almost constant behavior of Θ_0 is obtained, varying linearly, as indicated by the linear fit to the experimental data. At $D/L = 0.2$ a somewhat stronger dependency on U_∞ is found, though Θ_0 still varies linearly with U_∞. All other cases ($D/L \geq 0.3$) were fitted with a power fit function of the form $y = cx^d$, by minimizing the $\mathcal{L}_2$-norm difference of the analytical function and the experimental data. For $D/L \geq 0.3$, the momentum thickness is largely independent of the intercavity distance. Interestingly, for the single cavity case, slightly larger values of Θ_0 are obtained than for the closely related double cavity case with $D/L = 1.0$, suggesting, that even though the cavities are far, the incoming flow is still affected by the presence of the second cavity.

The streamwise velocity profiles inside the double cavity domain are fitted to a hyperbolic sine (sinh) profile, borrowed from the analysis of a cylinder wake [21]. The analytical form of the hyperbolic sine profile reads
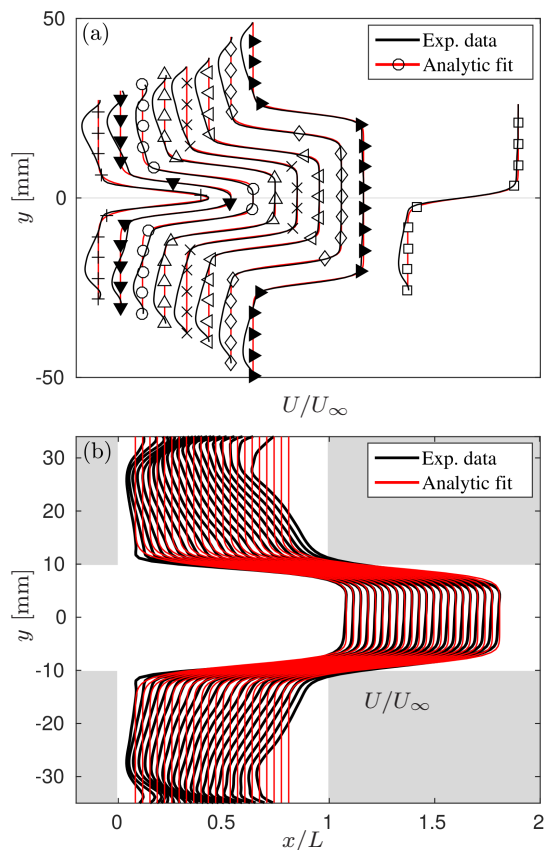

Fig. 9: Experimental and analytic velocity profiles (a) at streamwise position $x = x_{min}$ for all cases in table 1 at $Re_L \approx 9\,000$ and (b) along a double cavity with $D/L = 0.4$ at $Re_L = 8\,800$. The analytic profile is given in equation 5. Symbols as in table 1.

$$U_{sinh}(y, N, a) = \left[1 + \sinh^{2N}\left[y \sinh^{-1}(a)\right]\right]^{-1}, \qquad (5)$$

where $N \in \mathbb{N}$ and $a \in \mathbb{R}$ are the free parameters to be fitted. For the single cavity case the classical hyperbolic tangent (tanh) profile

$$U_{tanh}(y) = \frac{1}{2} + \frac{1}{2}\tanh\left(\frac{y}{2}\right) \qquad (6)$$

is proposed. Figure 9 shows the results of the fit for all cases in table 1, measured at $x = x_{min}$ for a Reynolds number of roughly $Re_L \approx 9\,000$. Again, the fit is performed by minimizing the $\mathcal{L}_2$-norm difference of the analytical profile and the experimental mean velocity profile, varying both N and a. The streamwise position x_{min} denotes the location where the best fit (in the least square sense) is obtained. More details on x_{min} can be found in section 5. In the channel center and the shear layer region good agreement between the analytic and
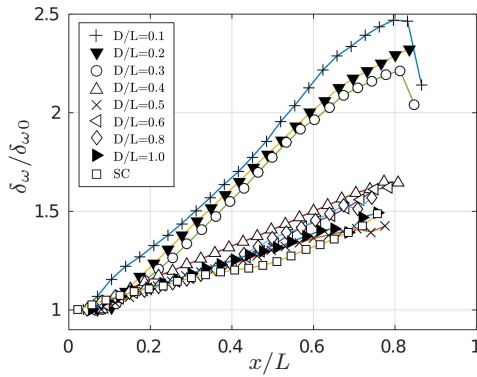
Fig. 10: Normalized vorticity thickness $\delta_\omega/\delta_{\omega 0}$ for all cases in table 1 at $Re_L \approx 9\,000$ computed from experimental data.

Fig. 11: Power spectra at multiple probe locations inside the double cavity case at $D/L = 0.5$ and $\mathrm{Re}_L = 9\,600$.

experimental profiles is observed for all intercavity distances. The recirculation regions inside both cavities are not captured by the sinh profile.

Figure 9(b) exemplifies for a case with $D/L = 0.4$ at $Re_L = 8\,800$ the development of the streamwise velocity profile along the double cavity, together with the fitted sinh profile. In the channel center the sinh profile follows closely the experimental data at all streamwise positions. Very close to the leading edge ($x/L < 0.15$) as well as close to the trailing edge ($x/L > 0.6$) both profiles show differences in the shear region, while close to the streamwise position x_{min} good agreement is obtained over the entire shear region. As mentioned before, inside the cavities we observe a difference between the experimental and the analytical profiles due to the recirculation regions which are not modeled by the sinh profile.

The vorticity thickness, defined as

$$\delta_\omega = \frac{\Delta U}{\left(\frac{\partial U}{\partial y}\right)_{\max}}, \tag{7}$$

is calculated along the cavity length from experimental velocity profiles for all cases in table 1 at $Re_L \approx 9\,000$. The inflexion point is determined such that the gradient ($\partial U/\partial y$) is maximum. The shear-strength is given as $\Delta U = U_{\max} - U_{\min}$. The vorticity thickness δ_ω, normalized with the vorticity thickness at the cavity's leading edge ($\delta_{\omega 0} = \delta_\omega(x = 0)$), is depicted in figure 10. The vorticity thickness at the cavity's leading edge $\delta_{\omega 0}$ is essentially determined by the momentum thickness Θ_0 of the incoming flow. The development along the double cavity domain was found to be largely independent of the Reynolds number, but strongly dependent on the intercavity distance. For intercavity distances
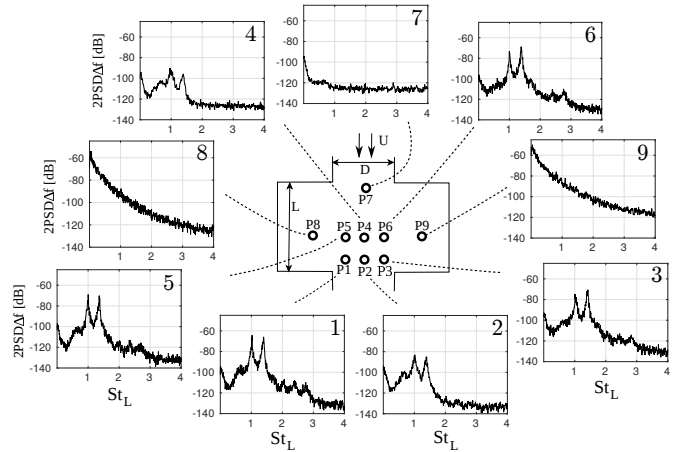
$D/L \leq 0.3$ the vorticity thickness δ_ω increases much stronger compared to larger distances and the value of δ_ω at $x/L = 0.8$ is roughly 50% higher. The trend is close to linear up to $x/L \approx 0.8$, where it flattens out and even drops due to the effect of the rear cavity edge. For intermediate distances $0.4 \leq D/L \leq 0.8$ the vorticity thickness starts showing a plateau-like zone between $0.2 \leq x/L \leq 0.5$. All cases at these distances show similar values. The plateau flattens out for increasing distances ($D/L = 1.0$ and SC), as was also found for the single cavity case by [1]. For the cases where the inflow profile corresponds to a Blasius boundary layer profile ($D/L \geq 0.3$), the value of $\delta_{\omega,0}$ at the cavities leading edge is $2\delta_{\omega,0} \approx 4.5\Theta_0$, which reasonably satisfies the theoretical properties of Blasius profile mixing layers, as defined by Huerre and Monkevitz [8]. A similar value ($2\delta_{\omega 0} \approx 4.6\Theta_0$) was found by Ref. [22] for the single cavity.

4 Spectral analysis

4.1 Probe positions and spectra

Figure 11 shows spectra recorded with Laser Doppler Velocimetry (LDV) at nine different probe locations inside the double cavity domain, for a case with $D/L = 0.5$ at $Re_L = 9\,600$. As expected, the spectrum at the inflow (P_7) shows no significant spectral content. Only a very low frequency peak at $St_L \approx 0$ is present, which is, as mentioned by [23], most likely due to steady features of the flow. The six probe points located in the channel center show the same spectral structure: two non-harmonic frequency peaks at Strouhal numbers $St_L \approx 1.0$ and $St_L \approx 1.4$, together with its first harmonics, which are roughly two orders of magnitude smaller in

amplitude. A rather broadband peak, one order of magnitude smaller, is found at around $St_L \approx 0.6$. The low frequency content at $St_L \approx 0$ is transmitted from the inflow. Probe points P_8 and P_9 are located inside the respective cavities. Spectra from times series recorded at these probe points are different from spectra recorded at probe points, located in the channel center. Only a strongly amplified broadband low frequency peak at $St \approx 0$ can be found in the power spectra of the intracavity probe points. The typical shear layer peaks can not be found. This is in agreement with Ref. [1], who found the same spectral structure inside the cavity of single open cavity flow at nearly the same Reynolds number and for the same cavity aspect ratio. In the present work we are mainly interested in the interaction of the two shear layers. Since probe points P_1 to P_6 give very similar results we will focus on time series recorded at probe point P_1 (which is coincident with the position of P_{LDV} in figure 3).

4.2 Local spectra

Time series for a wide range of Reynolds numbers and intercavity distances were recorded at point P_{LDV}. Figure 12 summarizes the power spectra of these time series in terms of the Strouhal number St_L, for the nondimensional intercavity distance D/L and Reynolds Re_L. The light gray checkered areas indicate the four cases, that were selected for a detailed spectral analysis in section 4.2.5. Different spectral compositions, depending on the intercavity distance and the Reynolds number, are observed. For sufficiently low Reynolds numbers all cases are in a (quasi) steady regime, where no significant shear layer oscillations are present.

By increasing the Reynolds number, the typical shear layer peak at $St_{L,1} \approx 1$ arises in all cases, except the very close distance case $D/L = 0.1$ (figure 12(a)). For $D/L \geq 0.2$ at increased Reynolds number a second nonharmonic peak at $St_{L,2} \approx 1.4$ appears. Both peaks exhibit a similar amplitude over a restricted Re-range, before $St = 1.4$ becomes the unique dominant peak in the spectrum. For a given Reynolds number the dominance between the two peaks switches as D/L is decreased down to $D/L = 0.4$. The switching scenario remains true for $D/L < 0.4$, though with much wider peaks. The lowest threshold to shear layer oscillations is found at the intermediate distance $D/L = 0.5$. For both, close distances ($D/L = 0.1$) and very far distances the shear layer oscillations arise at a roughly 25% higher Reynolds number than the one corresponding to this intermediate distance. We will consider in next section the spectra in the experimental conditions for which oscillations of the shear layers are significant.

4.2.1 Single Cavity Spectra

Figure 12(i) shows the spectra for a single cavity case as a reference to the eight double cavity cases depicted in figures 12(a)-(h). The results of the single cavity agree well with other works in literature, such as [22]. The peak associated with single shear layer oscillations at $St_{L,1} \approx 1$ is observed when a certain threshold in the Reynolds number is crossed. For even higher Reynolds numbers a bi-periodic regime takes place, where two, non-harmonic frequencies coexist. From the literature [3,22] we know, that for increasing L/Θ_0, the amplitude of the second peak at $St_{L,2}$ can even overtake the first peak at $St_{L,1}$. As shown in Ref. [22], this cascade process can reach up to $3St_{L,1}$ and $2St_{L,2}$ and is predominantly influenced by the term L/Θ_0. In our study, the takeover of the second peak is not observed for the single cavity but as we will see below, this phenomenon appears when approaching both cavities.

4.2.2 Spectra of intermediate to far intercavity distances

Let us consider the range of intermediate to far intercavity distances $0.4 \leq D/L \leq 1$, depicted in figures 12(d)-(h). At these distances, the spectral composition of the double cavity cases is similar to the one of the single cavity (figure 12(a)). The single shear layer peak at $St_{L,1} \approx 1$ is observed over a wide range of Reynolds numbers, that increases with D/L. For increasing Reynolds numbers the bi-periodic regime appears and the second non-harmonic frequency peak at $St_{L,2} \approx 1.4$ grows with increasing Re_L. The onset of the second peak continually increases with D/L. At $D/L = 0.4$ the Reynolds number of the onset is about 50% lower than for the single cavity. The peak of $St_{L,2}$ is less sharp than the one associated with $St_{L,1}$. The takeover of the second peak is observed for this intercavity distances range. This seems to indicate that the proximity of the second cavity advances the cascade process. For cases at $0.4 \leq D/L \leq 0.6$, this even leads to the disappearance of the first peak $St_{L,1}$ at the highest Reynolds numbers. Partly, this may be due to the decreasing value of Θ_0 (increasing value of L/Θ_0) with decreasing D/L, as shown in figure 8).

4.2.3 Spectra of close intercavity distances

For intercavity distances $D/L = 0.2$ and $D/L = 0.3$ (12(b)-(c)) the spectral composition changes drastically with respect to the single cavity. The steady regime is still followed by a periodic regime with a frequency peak at $St_{L,1} \approx 1$, however, the peaks are much broader.
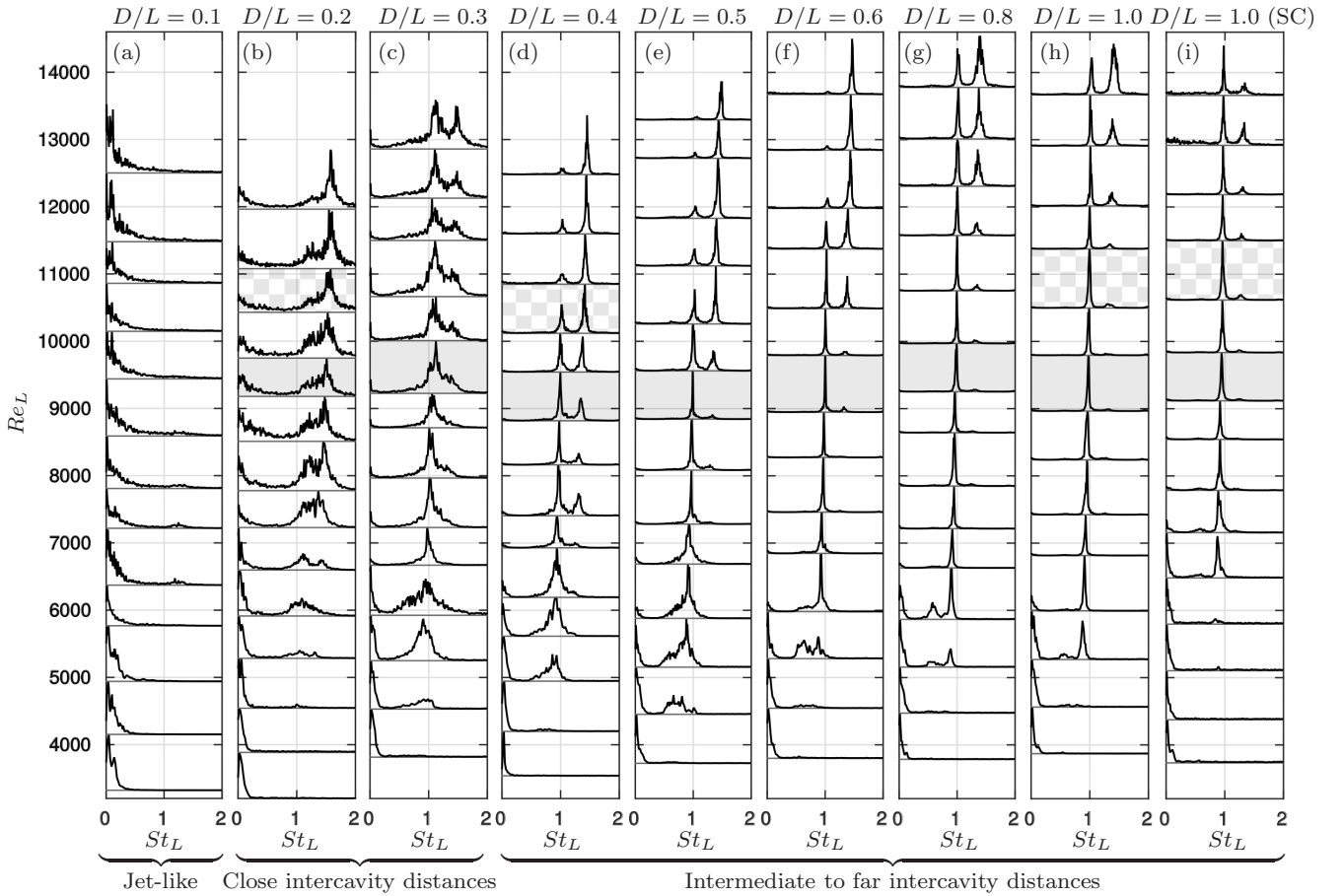
Fig. 12: Normalized power spectra PSD/max(PSD). The cases indicated by the checkered area are discussed in detail in section 4.2.5. The light gray shaded areas indicate cases for which a local temporal linear stability was carried out in section 5.

At a distance of $D/L = 0.3$ the second peak ($St_{L,2}$) eventually starts growing, though at a Reynolds number roughly 30% higher than for the neighboring case at $D/L = 0.4$. Both peaks show a similar increase in bandwidth. For the distance $D/L = 0.2$ the peaks broaden further and the second peak ($St_{L,2}$) overtakes the first peak ($St_{L,1}$) at a much lower Reynolds number, compared to the other cases. With decreasing intercavity distance, the frequency of both peaks increases continuously such that the following two inequalities hold:

$$St_{L,1}(SC) \leq St_{L,1}(D/L = 0.3), \tag{8}$$
$$St_{L,2}(SC) \leq St_{L,2}(D/L = 0.2). \tag{9}$$

4.2.4 Jet-like behavior

As mentioned above, at the closest intercavity distance $D/L = 0.1$ (12(a)), a significantly different spectral composition is observed. The flow type is called *jet-like*, as it is similar to the confined jet flow, investigated

at lower Reynolds numbers by Maurel et al. [18]. For all Reynolds numbers low frequency content dominates the spectra. Only between $6\,000 \lesssim Re_L \lesssim 9\,000$ a subtle peak at $St_L = 1.25$ appears. which is in accordance with mode III found by Maurel et al. [18].

As shown in section 3, due to the close intercavity distance, the double Blasius profile turns into a parabolic inflow profile. The resulting jet becomes unstable and, under the influence of the recirculation region, starts to flap irregularly at frequencies, that are one order of magnitude smaller than those of the typical shear layer oscillations. The unstable jet fluctuations can also be observed in the smoke visualizations provided in the supplementary material.

4.2.5 Detailed spectral composition

We will now analyze the composition of four typical spectra at different distances focusing on frequencies close to $St_{L,1}$ and $St_{L,2}$. Figure 13 shows a detailed
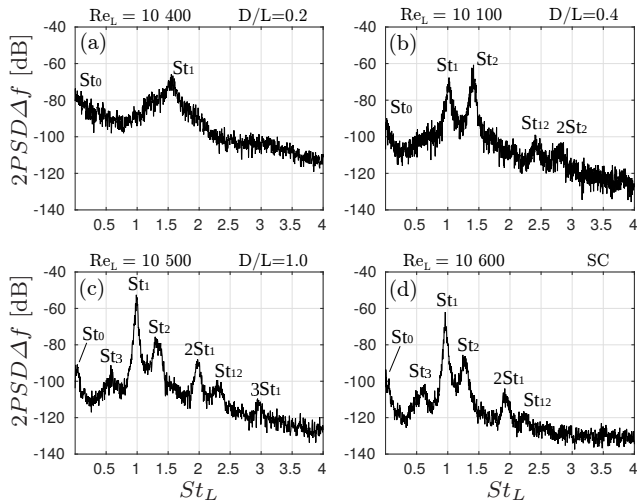
Fig. 13: Shear layer spectra recorded in probe point P_{LDV} for cases at (a) $D/L = 0.1$, (b) $D/L = 0.4$, (c) $D/L = 1.0$ and (d) SC at indicated Reynolds numbers, where $P = 2PSD\Delta f$ is the normalized power spectral density.

view of power spectra for four cases with comparable Reynolds numbers ($10\,100 \leq Re_L \leq 10\,600$) but different intercavity distances. As we see the logarithmic scaling reveals a rich composition of the spectrum.

The spectrum of the single cavity, shown in figure 13(a), exhibits a main frequency peak very close to the typical shear layer frequency at $St_1 = 0.96$. A second, about one order of magnitude less energetic, non-harmonic frequency peak can be found at $St_2 = 1.28$. The first harmonic of St_1 can be found at $2St_1 = 1.92$. St_{12} and St_3 are combinations of the two non-harmonic peaks and its harmonics: $St_{12} = St_1 + St_2 = 2.22$ and $St_3 = 2St_1 - St_2 \approx 0.6$. A low frequency peak at $St_0 \approx 0$ is common to all four cases.

When a second cavity faces the first cavity, the structure of the spectrum stays largely the same. The spectrum of a case with $D/L = 1$ is shown in figure 13(b). The second cavity acts like an amplifier, leading to a similar but more amplified spectrum, when compared to the single cavity case. The main peak at $St_1 = 0.99$ increases slightly and moves closer to unity. The second non-harmonic peak also increases slightly to $St_2 = 1.32$. All other peaks are again harmonics or linear combinations of these two peaks: $St_3 = 2St_1 - St_2 = 0.58$ and $St_{12} = St_1 + St_2 = 2.30$. Due to the increased amplification, even the third harmonic $3St_1 = 2.94$ can now be observed.

We consider now cases in which cavities are brought even at closer distances. At $D/L = 0.4$ we note, that the two non-harmonic peaks at $St_1 = 1.02$ and $St_2 = 1.41$ further increase in Strouhal number, as proposed earlier in inequalities 8 and 9, respectively. The amplitudes of both peaks are now within the same order of magnitude. In fact, the second peak even overtakes the first peak, showing the advancement in the cascade process, mentioned earlier in this section. As before, linear combinations of the two non-harmonic peaks are present: we find the second harmonic of the second peak at $2St_2 = 2.83$ and the sum of the two non-harmonic peaks at $St_{12} = St_1 + St_2 = 2.43$. We note that the peak at St_3 disappears and the peak-to-noise-ratio decreases, while both peaks broaden a little.

For even closer distances the spectrum changes strongly. The only prevailing two peaks are the low frequency peak at $St_0 \approx 0$ and the second shear layer peak at $St_2 = 1.54$. The latter broadens strongly, extending over roughly $\Delta St = 1$. Sideband peaks cannot be clearly identified most likely due to a further decrease of the peak-to-noise-ratio.

This sections has allowed us to synthesize the richness of the dynamics of the double cavity flow with the usual tool of spectral analysis. It is of interest to try to gain some physical insight of the phenomena involved with the use of other tools. Therefore we propose in next section to undertake a linear instability analysis with the hope this will provide a better understanding of the complex flow behavior. It is obvious however that the experimental results, we have shown, will not be fully described by such a simple analysis and complementary works are still required.

5 Temporal linear stability analysis

5.1 The considered model

In this section, we present the results of a temporal linear stability analysis. Our goal is to try to explain why the frequency peaks for close intercavity distances ($D/L = 0.2$ and $D/L = 0.3$) show stronger side bands (broadening of the peaks) and move away from the classical shear layer peak value of $St_L \approx 1$.

The flow is assumed to be steady, parallel and unidirectional. The streamwise development of the base flow is therefore entirely neglected. The analysis of flow stability considers the two-dimensional, inviscid and incompressible Euler equations given by
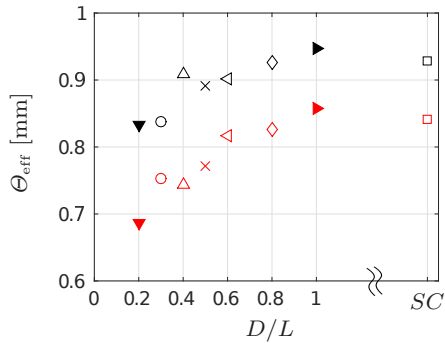
Fig. 14: Effective momentum thickness Θ_{eff} over distance D for all cases in table 2, computed from analytic profiles (black) and from experimental profiles (red). Symbols as in table 2.

$$\partial_t \mathbf{u} + [\mathbf{u} \cdot \nabla]\mathbf{u} = -\nabla p \qquad (10)$$
$$\nabla \cdot \mathbf{u} = 0, \qquad (11)$$

where $\mathbf{u} = (u, v)^T$. The flow variables $\mathbf{q}(x, y, t) = (u, v, p)^T$ and coordinates x, y are non-dimensionalized using the maximum velocity U_∞ and the effective momentum thickness Θ_{eff} as in Ref. [9]. In accordance with Ref. [8], the effective momentum thickness is computed from the velocity profiles at the streamwise position $x = x_{min}$, defined later in this section. The flow is decomposed into a steady laminar base flow $\overline{\mathbf{Q}}(y) = (\overline{U}, \overline{V}, \overline{P})^T$ upon which small amplitude perturbations $\mathbf{q}'(\mathbf{x}, t) = (u', v', p')^T$ are permitted ($\mathbf{x} = (x, y)^T$). Normal mode solutions $\mathbf{q}'(\mathbf{x}, t) = \hat{\mathbf{q}}(y)e^{i(kx - \omega t)}$ with $\hat{\mathbf{q}}(y) = (\hat{u}, \hat{v}, \hat{p})^T$ are then considered to model the temporal development of the perturbations. Note, that the wave number k and the angular frequency ω are also non-dimensionalized using the maximum velocity U_∞ and the effective momentum thickness Θ_{eff}. The decomposed flow field is subsequently linearized by neglecting higher order perturbation terms. This yields a system of linear equations, which in the case of the temporal linear stability analysis is solved as an eigenvalue problem (EVP) for a real wave number k_r, resulting in a complex frequency $\omega = \omega_r + i\omega_i$. The complex part of the frequency ω_i corresponds to the temporal growth rate and the real part of the frequency ω_r to the physical frequency.

The boundary conditions of the EVP for $\mathbf{u}$ are of Dirichlet type (no-slip conditions at the solid walls) at $y = \pm(H^* + D^*/2)$, where H^* and D^* are the with the effective momentum thickness normalized cavity depth and channel height, respectively. The boundary condition for the pressure is of Neumann type, as follows from the momentum equation. The customary parallel

Table 2: Summary parameters of linear stability analysis

Cases	D/L	a	N	Re_L	Symbol
DC10	0.2	2.28	2	9 200	▼
DC15	0.3	2.68	3	9 300	○
DC20	0.4	3.04	4	8 800	△
DC25	0.5	3.23	5	8 900	×
DC30	0.6	3.43	6	9 000	◁
DC40	0.8	3.74	8	9 300	◇
DC50	1.0	3.98	10	9 000	▶
SC50	1.0	—	—	9 100	□

flow assumptions $\overline{V} = 0$, $\overline{P} = \text{const}$ and $\partial_x \overline{Q} = 0$ are applied. The one dimensional base-state of the velocity field $\overline{U} = f(y)$ is non-dimensionalized with the centerline (or freestream) velocity U_∞ and the effective momentum thickness Θ_{eff}, shown in figure 14. For the double cavity cases the sinh velocity profile from equation 5 is fitted to the experimental data by minimizing the $\mathcal{L}_2$-norm difference of experimental streamwise velocity profile and the analytical profile, varying the fitting parameters a and N. For the single cavity case the classical tanh profile (equation 6) is used. The analytic fits to the experimental velocity profiles which are imposed on the dispersion relation of the linear stability analysis are depicted in figure 9(a). The momentum thickness of the fitted analytic velocity profiles is compared to the experimental values in figure 14 for all analyzed cases. While the trend is well captured by the fitted profiles, the absolute values lie slightly above the experimental values of Θ_{eff}. The streamwise position, at which the experimental velocity profiles as well as the effective momentum thickness are taken, is denoted $x = x_{min}$. At this position the error between the analytic and the experimental profile, given by

$$E(x_{min}) = \min(|U_{sinh}(y) - U_{exp}(y)|^2), \qquad (12)$$

yields a minimum. In agreement with Refs. [8] and [9], the position x_{min} was found close to $x_{min} \approx 0.25\,L$ in all cases.

The EVP together with the base-flow assumptions yield the dispersion relation of the system, given by the complex equation

$$\Delta(\omega_r, \omega_i, k_r) = 0 \qquad (13)$$

For a real wavenumber k_r, the roots $\omega(k)$ of this equation provide the eigen-frequencies and temporal growth rates. The dispersion relation is solved numerically using a Matlab code based on an adapted Chebyshev collocation method, which refines the grid points in both shear layers zones, in order to guarantee a high
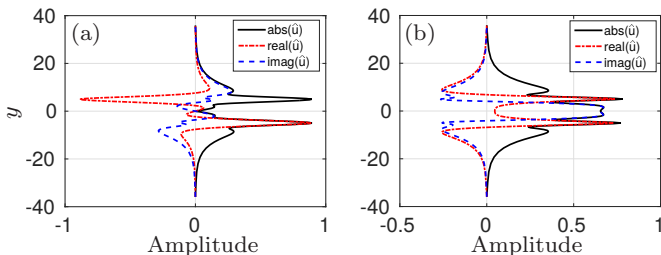
Fig. 15: Eigenmodes from case DC10 ($D/L = 0.2$) at $\omega_{i,max}$ for (a) sinuous mode (more amplified) (b) varicose mode (less amplified).
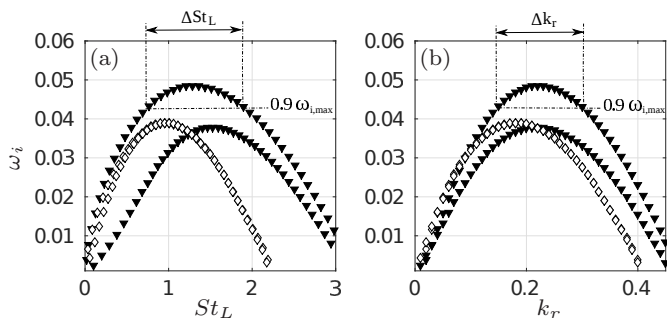

Fig. 16: Linear stability curves for cases DC10 ($D/L = 0.2$, ▼) and DC40 ($D/L = 0.8$, ◊). For the definition of the Strouhal number range ΔSt_L and the wave number range Δk_r see main text.

resolution in areas with strong velocity gradients. Between $M = 100 - 120$ grid points were used, depending on the case. Differentiation is carried out using a second order non-equidistant finite difference method. The fitting parameters N and a of each case are summarized in table 2. The effective momentum thickness Θ_{eff}, depicted in figure 14, increases with D/L. The Strouhal number St_L is obtained by

$$St_L = \frac{fL}{U_\infty} = \omega_r \frac{U_\infty}{\Theta_{\text{eff}}} \frac{1}{2\pi} \frac{L}{U_\infty} = \omega_r \frac{L}{2\pi \Theta_{\text{eff}}} \qquad (14)$$

where ω_r is the non-dimensional angular frequency resulting from the linear stability analysis. The Strouhal number is independent of the inflow velocity and only depends on the momentum thickness Θ_{eff} and the cavity length L. The momentum thickness appears due to its use as the normalizing scale in the stability analysis while the cavity length serves as a limiter for the preferred frequency of oscillation, in accordance with other works in the literature [15,18,9], who expect that a certain number of wavelengths, or fraction thereof, must enter the cavity. The light gray shaded areas in figure 12 indicate the cases, for which the linear stability analysis was carried out.

5.2 Results and Discussion

As in Ref. [21], the temporal linear stability analysis of the sinh profile results in two unstable branches: a symmetric (varicose) and a anti-symmetric (sinuous) branch. Figure 15 exemplifies both eigenmodes for case DC10 ($D/L = 0.2$). The tanh profile results in a single (sinuous) branch, which is in accordance with Ref. [6].

Figure 16(a) shows the temporal amplification rate ω_i over the Strouhal number St_L, exemplary for two cases: a close distance case at $D/L = 0.2$ and a far distance case at $D/L = 0.6$. At $D/L = 0.2$ the two branches are well separated. The sinuous branch yields higher values of ω_i and hence is more unstable. The difference between the branches decreases with distance, such that for distances $D/L \geq 0.4$, the difference between the two branches becomes negligible and both modes exhibit a similar temporal amplification rate ($\Delta\omega_i < 3\%$), i.e. both modes are equally prone to amplification. These theoretical predictions are in good agreement with the experimental results from the shear layer correlations in section 3 (figure 6), where we found, that for small intercavity distances, the flow is anti-symmetric from a spatio-temporal point of view, while for larger intercavity distances ($D/L \geq 0.4$) symmetry is lost.

We define the Strouhal number St_L, at which the growth rate ω_i is maximal, as

$$St_{L,max} = St_L(\omega_{i,max}) \qquad (15)$$

and in the same manner the wave number k_r, at which the growth rate ω_i is maximal, as

$$k_{r,max} = k_r(\omega_{i,max}) \qquad (16)$$

In figure 16, the temporal growth rate is plotted as a function of the Strouhal number and the wave number. When the two branches are distinguishable, $St_{L,max}$ of the varicose branch is found at higher Strouhal numbers than $St_{L,max}$ of the sinuous mode. The wave number of the maximal growth rate $k_{r,max}$, however, is found to be equal for the two branches, as can be seen from figure 16(b).

Figure 17 summarizes the results from the linear stability analysis for all eight cases in table 2 and compares them to the experimental data from section 4. The Strouhal number of the maximum growth rate $St_{L,max}$, the Strouhal number range ΔSt_L, the wave number range Δk_r and the maximum growth rate $\omega_{i,max}$ are plotted over the non-dimensional intercavity distance

D/L. The Strouhal number range and the wave number range are defined as

$$\Delta St_L = \{St_L \in \mathbb{R} \mid 0.9\,\omega_{i,max} \leq \omega_i(St_L) \leq \omega_{i,max}\} \quad (17)$$

$$\Delta k_r = \{k_r \in \mathbb{R} \mid 0.9\,\omega_{i,max} \leq \omega_i(k_r) \leq \omega_{i,max}\} \quad (18)$$

Figure 16 exemplifies the definitions for the case $D/L = 0.2$. The experimental values of the Strouhal number range and the wave number range were obtained from the power spectra, considering a cut-off threshold according to

$$\Delta St_L = \{St_L \in \mathbb{R} \mid P(St_L) > -85\text{dB}\} \quad (19)$$

$$\Delta k_r = \{k_r \in \mathbb{R} \mid P(St_L) > -85\text{dB}\} \quad (20)$$

where $P = 2PSD\Delta f$ is the normalized power spectral density.

In figure 17(a), at $D/L = 0.2$, the value of $St_{L,max} = 1.37$, obtained by the linear stability analysis, is slightly below the experimental value of $St_{L,max} \approx 1.5$. At the distance $D/L = 0.3$, the linear stability analysis predicts $St_{L,max} = 1.26$, while experimentally we obtain a somewhat lower value of $St_{L,max} \approx 1.12$. Experimentally, for $D/L \geq 0.4$, the frequency peaks become more narrow band and start to be distinguishable. The experimental data for $D/L \geq 0.4$ shows the amplification of two non-harmonic peaks, $St_{L,1}$ (red) and $St_{L,2}$ (blue). For cases with $0.3 \leq D/L \leq 0.6$, the first mode $St_{L,1}$ lies below the value obtained from the linear stability analysis, while the second mode $St_{L,2}$ is found at a higher Strouhal number. The far distance cases $0.8 \leq D/L \leq 1.0$ coincide well with the first experimental mode $St_{L,1}$, found close to unity. For the single cavity (SC), the predicted value $St_{L,max}$ of the linear stability analysis increases slightly to $St_{L,max} = 1.1$ and lies exactly in between the values obtained experimentally ($St_{L,1} = 0.96$ and $St_{L,2} = 1.24$). This is in agreement with Ref. [9], who found that, in order to predict both non-harmonic peaks, the finiteness of the system has to be taken into account.

In figure 17(b)-(c), the Strouhal number range ΔSt_L and the wave number range Δk_r are depicted. As found in section 4, for close intercavity distances, $0.2 \leq D/L \leq 0.3$, the frequency peaks broaden, $i.e.$ a greater range of frequencies is amplified. This is reflected in the increased value of ΔSt_L. The results from the linear stability analysis compare well to the experimental data. For intermediate distances $0.4 \leq D/L \leq 0.6$ both the linear stability prediction and the experimental data show a drop in ΔSt_L, however, the amplified frequency range of the experimental data drops stronger than the linear stability analysis predicts. The arbitrary frequency range selection criterion ($0.9\,\omega_{i,max}$) could be
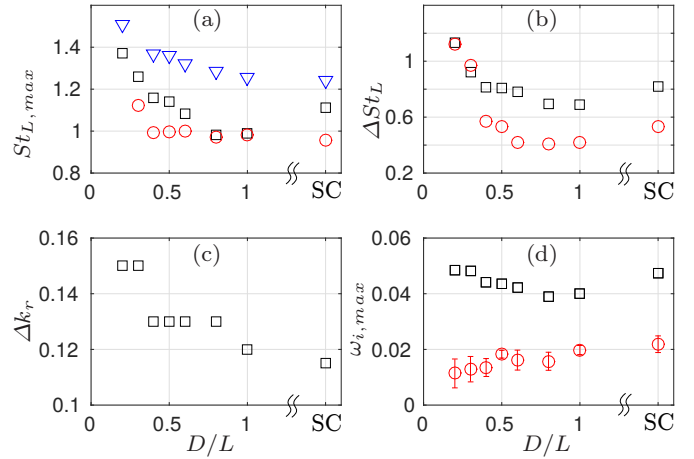

Fig. 17: Results from linear stability analysis compared to experimental results for different intercavity distances D/L and the single cavity (SC). (a) Strouhal number of the first experimental mode $St_{L,1}$ (red ○), the second experimental mode $St_{L,2}$ (blue ▽) and linear stability analysis (black ☐). (b) Strouhal number range ΔSt_L, (c) wave number range Δk_r and (d) maximum growth rate $\omega_{i,max}$ from experimental results (red ○) and from linear stability analysis (black ☐). Error bars in (d) indicate 95% confidence interval of the fitted growth rate $\omega_{i,exp}$ (equation 22).

adapted to increase the accuracy. The rebound of ΔSt_L for large intercavity distances $D/L \geq 0.8$ and the single cavity, found experimentally, is also predicted by the linear stability analysis. The wave number range Δk_r, depicted in figure 17(c), shows a nearly linear and monotonic decrease with D/L. This suggests, that a closer intercavity distance is favorable to a greater set of wave numbers being amplified. In figure 17(d), the maximum temporal growth rate $\omega_{i,max}$, obtained from the linear stability analysis, also decreases with D/L, however, only up to a distance of $D/L = 0.8$. For $D/L > 0.8$ it increases again and finally settles for the single cavity at almost the same value as at close intercavity distances.

In order to compare the temporal growth rates of the linear stability analysis to the experimental results from section 3, the experimental temporal growth rates are calculated for all cases in table 2. In figure 18 the rms (root-mean-square) peak values $A(x)$ of the streamwise fluctuating velocity component are plotted over the cavity length in a range of $0.2 \lesssim x/L \lesssim 0.6$, exemplary for three cases. The maximum value at each streamwise position is normalized with $A(x_0)$, where $x_0 \approx 0.2\,L$. For $x < x_0$ the velocity profiles are stable and no significant shear layer fluctuations are observed.
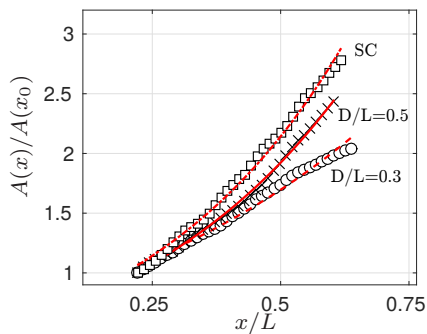
Fig. 18: Amplitude of rms (root-mean-square) of fluctuating streamwise velocity component over cavity length exemplary for cases $D/L = 0.3$ ($\circ$ and $--$), $D/L = 0.5$ ($\times$ and $—$) and single cavity SC ($\square$ and $-\cdot-$). Symbols show experimental data, curves indicate exponential fits.

For $x/L \gtrsim 0.6$ nonlinearities saturate the fluctuations. An exponential function of the form

$$A(x) = \gamma\, e^{\kappa x} \tag{21}$$

is fitted to the experimental data by minimizing the $\mathcal{L}_2$-norm difference, varying the fitting parameters γ and κ. After normalization with the maximum center line velocity U_∞ and the effective momentum thickness Θ_{eff}, we obtain the temporal growth rate according to

$$\omega_{i,exp} = \kappa c_g \frac{\Theta_{\mathrm{eff}}}{U_\infty} = \kappa \frac{\Theta_{\mathrm{eff}}}{2} \tag{22}$$

where $c_g = \frac{\partial \omega}{\partial k}$ is the group velocity of the perturbing wave packet, which was found to be $c_g \approx 0.5\, U_\infty$, independent of the intercavity distance. Figure 18 exemplifies the fitting procedure for three cases. Interestingly, at close distances ($D/L \leq 0.4$) the amplitude of the streamwise velocity fluctuations increases nearly linearly along the cavity length. For larger distances ($D/L \geq 0.5$) the typical exponential growth is observed and equation 21 fits well the experimental data. The proximity of the facing cavity seems to inhibit the exponential growth of fluctuations. In figure 17(d) the experimental growth rates $\omega_{i,exp}(x)$, calculated according to equation 22 for all cases in table 2 are compared to the maximum temporal growth rates $\omega_{i,max}$, obtained from the linear stability analysis. As expected from an inviscid analysis, the experimental growth rates are found at somewhat lower values than the theoretical predictions but within the same order of magnitude. For close intercavity distances the trend of the predictions does not resemble the experimental data. This is due to the linear course of $A(x)$ for $D/L \leq 0.4$, which reduces

$\omega_{i,exp}$. For distances $D/L \gtrsim 0.5$, independent of the intercavity distance, similar growth rates of approximately $\omega_{i,exp} \approx 0.02$ are obtained.

Note, the temporal linear stability analysis only predicts a single frequency peak, while experimentally for certain parameters two non-harmonic peaks are observed. Recently Tuerke et al. [9] showed that taking into account the finite extent of the system results in a quantization mechanism of the frequency spectrum. This, so called linear stability analysis in a finite domain, was able to explain the existence of non-harmonic frequency peaks in the shear layer spectrum and is a suitable candidate for the double cavity geometry. It is subject of current on-going research work.

6 Conclusion

We report experimental and analytical results of the flow through two facing identical cavities, namely a double cavity, as the Reynolds number and the intercavity distance are varied. Experimentally, the flow was studied by means of non-time resolved PIV (particle image velocimetry) and time resolved LDV (laser Doppler velocimetry) measurements. The streamwise velocity profiles inside the double cavity were found to fit well a hyperbolic sine (sinh) profile intercavity distances $D/L \geq 0.2$. For the distance $D/L = 0.1$ the streamwise velocity profile in the inflow channel yields a parabolic profile. At such close distance the shear layers, forming over each cavity merge along the double cavity length and the instantaneous flow fields show a fluctuating jet, oscillating between the two cavities. This flow configuration corresponds confined jet flow [18]. For $D/L \geq 0.2$ the two shear layers stay separated all along the cavity length. For close distances the flow is anti-symmetric from a spatio-temporal point of view, while for larger distances no symmetry could be observed. This observation was confirmed by the results of a temporal local linear stability analysis, which showed that for $D/L \geq 0.4$ the varicose and the sinous branch coincide.

Spectra, recorded at various probe locations inside the double cavity domain, reveal its global nature. From power spectra, recorded at a single probe point in the impingement zone of one of the shear layers for a wide range of distances and Reynolds numbers a parameters space plot was built. A steady, a periodic and a bi-periodic regime were observed as the Reynolds number is increased. The onset of the regimes change with the intercavity distance. At the closest intercavity distance ($D/L = 0.1$) the different flow structure, observed in the instantaneous fields, is confirmed by the

absence of the dominant shear layer frequency peaks. All other cases show strong spectral activity at the typical shear layer frequency $St_L \approx 1$. For intercavity distances $0.2 \leq D/L \leq 0.3$ the peaks broaden and move to higher Reynolds numbers. This observation was again confirmed by the results of a temporal local linear stability analysis, which showed that the range of amplified frequencies increases with decreasing distance. At distances $D/L \geq 0.4$, the spectral signature looks similar to the single cavity, though the bi-periodic regime, is reached at lower Reynolds numbers the smaller D/L. The difference between the temporal growth rate, predicted by the linear stability analysis, and the temporal growth rate, computed from the experimentally measured spatial growth rate, may be due to viscous effects, which were not taken into account by the inviscid Euler equations.

References

1. J. Basley, L. Pastur, F. Lusseyran, T. Faure, N.Delprat, Experiments in Fluids **50**(4), 905 (2010)
2. F. Lusseyran, L. Pastur, C. Letellier, Physics of Fluids **20**(114101) (2008)
3. J. Basley, Doctoral Thesis (2012)
4. C.W. Rowley, T. Colonius, A.J. Basuz, J. Fluid Mech. **455**, 315 (2002)
5. G. Bres, T. Colonius, J. Fluid Mech. **599**, 309 (2008)
6. A. Michalke, J. Fluid Mech. **19**, 543 (1964)
7. Landau, Lifschitz, *Physical Kinetics*, *Course of Theoretical Physics*, vol. 10 (Robert Maxwell, M.C., 1985)
8. P. Huerre, P. Monkewitz, J. Fluid Mech. **159**, 151 (1985)
9. F. Tuerke, D. Sciamarella, L.R. Pastur, F. Lusseyran, G. Artana, Physical Review E **91** (2015)
10. J. Rossiter, Internal Report Ministry of Aviation **3438** (1964)
11. E. Villermaux, E. Hopfinger, Physica D **72**, 230 (1994)
12. F. Tuerke, L. Pastur, Y. Fraigneau, D. Sciamarella, F. Lusseyran, G. Artana, Journal of Fluid Mechanics **813**, 1 (2017)
13. E. Chisari, G. Artana, D. Sciamarella, Experiments in Fluids pp. 397–406 (2010)
14. A. Powell, Acustica 3 pp. 233–243 (1953)
15. D. Rockwell, E. Naudascher, Ann. Rev. Fluid Mech. **11**, 67 (1979)
16. F. Alizard, J.C. Robinet, X. Gloerfelt, Computers and Fluids **66**, 63 (2012)
17. J. de Vicente, J. Basley, F. Meseguer-Garrido, J. Soria, V. Theofilis, J. Fluid Mech. pp. 189–220 (2014)
18. A. Maurel, P. Ern, B.J.A. Zielinska, J.E. Wesfreid, Physical Review E **54(4)**, 3643 (1996)
19. T. Morel, Journal of Fluids Engineering **101** (1979)
20. P.D. Welch, IEEE Transactions on Audio and Electroacoustics **15** (1967)
21. P. Huerre, M. Rossi, *Hydrodynamics and Nonlinear Instabilities* (Camebridge University Press, 1998)
22. J. Basley, L.R. Pastur, N.Delprat, F. Lusseyran, Physics of Fluids **25** (2013)
23. J. de Vicente, J. Basley, F. Meseguer-Garrido, J. Soria, V. Theofilis, J. Fluid Mech. **748**, 189 (2014)
24. C. Ho, P. Huerre, Ann. Rev. Fluid. Mech. **16**, 365 (1984)
25. V. Sarhia, PhD Thesis p. 128 (1975)
26. D. Rockwell, Trans. ASME: J. Fluids Engeneering pp. 294–300 (1977)
27. D. Sciamarella, P.L. Quéré, European Journal of Mechanics B/Fluids **27/1**, 42 (2008)